Structural Reconstruction of the Graphene Monovacancy

Alex W. Robertson,[†] Barbara Montanari,[‡] Kuang He,[†] Christopher S. Allen,[†] Yimin A. Wu,[†] Nicholas M. Harrison,[‡] Angus I. Kirkland,[†] and Jamie H. Warner[†,*]

[†]Department of Materials, University of Oxford, Parks Road, Oxford OX1 3PH, United Kingdom and [‡]Rutherford Appleton Laboratory, Didcot, Oxfordshire OX11 0QX, United Kingdom

ABSTRACT Two distinct configurations of the monovacancy in graphene have been observed using aberration-corrected transmission electron microscopy (AC-TEM) at 80 kV. The predicted lower energy asymmetric monovacancy (MV), exhibiting a Jahn–Teller reconstruction (r-MV), has been observed, but in addition, we have imaged instances of a symmetric monovacancy (s-MV). We have used geometric phase analysis (GPA) to quantitatively determine the strain in the lattice surrounding these two defect configurations and show that the Jahn–Teller reconstruction generates significant extra strain compared to the symmetric MV case. Density functional theory calculations demonstrate that our experimental images of the two different monovacancies show good agreement with both the low energy r-MV and the metastable structures.

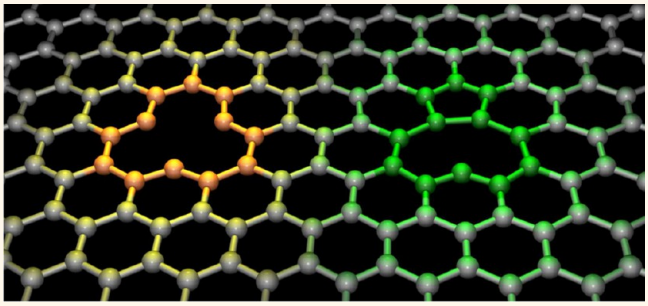

KEYWORDS: graphene · HRTEM · defects · TEM · electron microscopy

To usefully deploy graphene in electronic applications,[1−3] it is essential to understand the behavior of point defects. This has already been the subject of extensive research over the decades for silicon devices, due to the influence of vacancies on doping and semiconducting properties.[4,5] Prior to the development of graphene, irradiation studies of graphite surfaces constituted the bulk of established research into point defects in sp^2 carbon,[6−8] primarily motivated by the use of graphite in nuclear reactors.[9] This has more recently been extended to include studies of defects in carbon nanotubes[10] and has subsequently developed to include several theoretical studies demonstrating the magnetic character of certain graphitic defects.[11−14] It has been shown that the most fundamental of these defects, the monovacancy, can diffuse and coalesce to form more complex vacancy structures[15] and, as such, is a logical starting point for studies of graphene point defects.

The graphene monovacancy, formed by the ejection of a single carbon atom from the lattice, has been studied theoretically in graphene, carbon nanotubes, and graphite.[13,15−22] These have demonstrated that the monovacancy can exhibit a Jahn–Teller distortion, causing an initially symmetric monovacancy (s-MV) to reconstruct into a closed five- and nine-membered pair of rings. The s-MV configuration has three under-coordinated C atoms that each bond to only two neighbors, whereas the reconstructed monovacancy (r-MV) has been shown to lower the energy of the vacancy structure, due to a combination of the saturation of two initial dangling bond states in the reconstruction and an apparent out-of-plane displacement of the third under-coordinated C radical.[20] Prior studies of the monovacancy have relied on data from scanning tunneling microscopy (STM) studies of graphite and lacked the atomic resolution required to conclusively confirm the structure as symmetric or reconstructed.[7,8,20] With developments in high-resolution (HR) and, more recently, aberration-corrected transmission electron microscopy (AC-TEM),[23−27] it is now possible to characterize individual vacancy defects in graphene at atomic resolution, enabling the direct verification of theoretically predicted structures by experiment. A detailed understanding of the behavior of vacancies will be important for the practical exploitation of graphene in

* Address correspondence to jamie.warner@materials.ox.ac.uk.

Received for review March 5, 2013 and accepted April 11, 2013.

Published online April 16, 2013
10.1021/nn401113r

devices, with regard to how they influence local and long-range properties and in the potential for them to act as dopant sites.[12,28] Accordingly in this paper, we present studies of the graphene monovacancy observed by AC-TEM together with density functional theory (DFT) calculations to interpret the atomic structure.

RESULTS AND DISCUSSION

To create monovacancies, we have utilized our previously reported method of controllable defect creation, which uses a high current density electron beam of 80 kV to sputter a selected area of graphene for a predetermined exposure time.[26] This method for controlled defect creation allowed us to image multiple instances of monovacancy defects. Moreover, operating the AC-TEM at 80 kV, we were able to image the resultant graphene point defects at low beam current density while minimizing further radiation damage. The Oxford-JEOL 2200MCO fitted with CEOS third-order probe and image correctors was used to obtain atomic resolution images of graphene vacancies. Some images presented here (Figures 4a,e and 5h,i) were taken using a monochromated electron beam with ~0.3 meV energy width, providing sufficient spatial resolution to resolve individual atoms.[29] For the experiments reported here, chemical vapor deposition (CVD) graphene was used, synthesized according to ref 30, before transfer to a holey Si_3N_4 TEM grid by using a PMMA scaffold. Schematic atomic models were constructed within Accelrys Discovery Studio Visualizer, and AC-TEM image simulations were calculated using multislice method within the JEMS software.[31] AC-TEM images were subsequently filtered using a nearest neighborhood (3 × 3) operator to reduce high frequency noise. DFT calculations with the PBE functional[32] were conducted using the CRYSTAL code.[33,34] The numerical approximations adopted, and the triple valence with polarized local Gaussian basis set, have been described previously.[35] Defects were represented in a periodic 10 × 10 supercell of the graphene primitive unit cell. In the supercell, the eigensolutions were sampled on a 9 × 9 Pack-Monkhorst grid.

Following controlled defect creation, we observed both s-MV and r-MV defects by AC-TEM imaging. A smoothed AC-TEM image of a s-MV is shown in Figure 1a, with an accompanying DFT-calculated atomic model in Figure 1b. The multislice image simulation of the DFT-optimized geometry (Figure 1c) demonstrates good agreement with the experimentally observed structure, including regions of darker contrast on the three edge C atoms. We attribute this darker contrast to be an edge effect as previously described by Liu *et al.*[36] Figure 1d shows a smoothed AC-TEM image of a r-MV defect, together with a DFT atomistic model in Figure 1e and an image simulation in

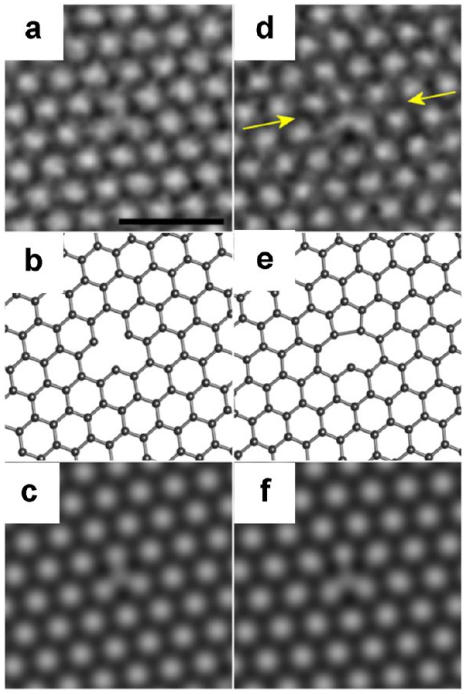

Figure 1. (a) Smoothed AC-TEM image of the symmetric monovacancy, s-MV, with three edge C atoms. (b) DFT-calculated atomistic model and (c) multislice TEM image simulation corresponding to the structure in (a). (d) Smoothed AC-TEM image of the reconstructed monovacancy, r-MV, with one edge C atom. Yellow arrows indicate the zigzag axis containing the reconstruction. (e) DFT-calculated atomistic model and (f) multislice TEM image simulation corresponding to the structure in (e). Scale bar corresponds to 1 nm in all panels.

Figure 1f. Figure 1f also shows good agreement with the experimental image in Figure 1d, including the darker contrast at the single under-coordinated C atom radical. In addition, the r-MV TEM image shows a contraction along the zigzag axis of the reconstruction (yellow arrows) compared to the s-MV exposure.

It is possible that the captured images of the s-MV correspond to a r-MV oscillating between the three stable r-MV configurations at sufficiently high frequency such that images integrated over a single exposure (2−3 s) lead to an averaged structure reminiscent of a s-MV. This model would be consistent with the STM data reported in ref 20, and thus it is prudent for us to consider if this model is also consistent with our defect images. To explore this, Figure 2a−c shows multislice TEM image simulations of a DFT model for the r-MV in each of the three possible 120° rotations, with the blue arrows marking the reconstructed bond. A simple equally weighted average of these images, implying no specific rotation preference, yielded the image shown in Figure 2d. This shows a good qualitative resemblance to the image of the s-MV in Figure 1a and to the multislice image simulation of the DFT optimized s-MV geometry in Figure 2e. Intensity line profiles measured between pairs of under-coordinated carbon atoms in Figure 2d,e are shown in Figure 2f,g,

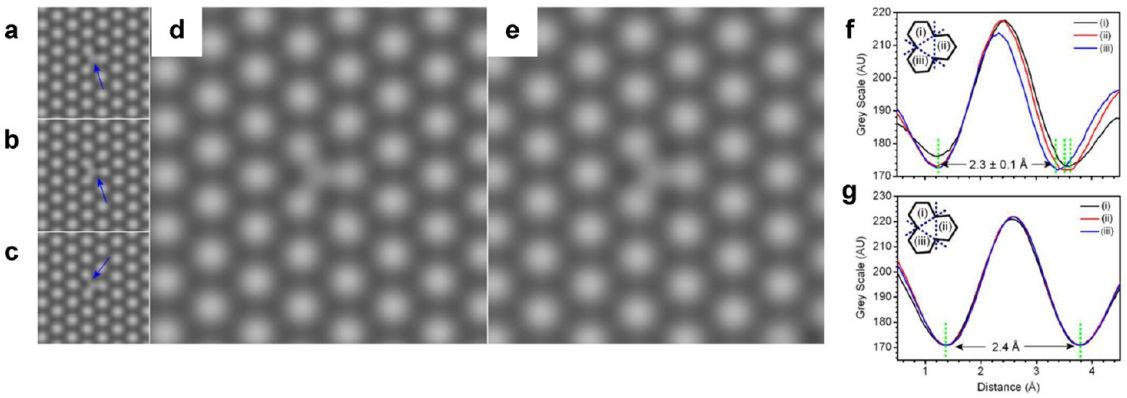

Figure 2. (a−c) Multislice image simulations of DFT modeled r-MV, rotated to align along the three different 120° zigzag axes (bond reconstruction denoted by the blue arrows). (d) Averaged image of the three rotated r-MV configurations in (a−c). (e) Multislice image simulation of a DFT-modeled s-MV. (f,g) Intensity profiles between the under-coordinated atoms in the averaged image in (d) and the DFT image in (e), respectively. Profiles are taken along the three zigzag axes that cross the gap between under-coordinated atom pairs, labeled (i−iii) as shown in the inset schematics.

which yield distances of 2.2−2.4 Å for the averaged image, in good agreement with the length of 2.4 Å in the s-MV image. This suggests that it is not possible to differentiate images of a metastable s-MV or superposed rotated r-MVs with the temporal recording resolution available.

Further insights can be gained by examining the time-dependent dynamics of the monovacancies under electron beam irradiation. We have seven separate image series where stable r-MV configurations were recorded, such as that shown in Figure 1d, which demonstrate that the reconstruction can be stable for time periods on the order of seconds, the time required for a single TEM exposure. This compares with five distinct image series of the s-MV defect. Furthermore, time series show stable r-MVs configurations that persist for significantly longer than a single exposure, with lifetimes in excess of 90 s (shown in Supporting Information Figure S1). The lifetime suggested in ref 20 for the reconstruction is 15 ps at room temperature, which is 11 orders of magnitude lower than the exposure times used here. Our results indicate that the r-MV does not necessarily undergo rapid oscillations between the three possible configurations and can lock into a stable orientation.

To demonstrate that it is possible to differentiate between images of the two types of MV configurations, geometric phase analysis (GPA) was applied to AC-TEM images of the defects. The GPA provides a strain field map of the area around the vacancy and is sensitive to local variations in the atomic structure.[37,38] Figure 3a−f shows GPA of the s-MV defect. Figure 3a shows a smoothed AC-TEM image of the s-MV used in the analysis, with a magnified inset highlighting the vacancy with a color look-up table (LUT) applied to enhance visual contrast. Figure 3b shows the Fourier transform (FT) calculated from Figure 3a, where the circled reflections denote the two Bragg reflections which are used for the GPA. Figure 3c−f shows the fields of the matrix elements of the symmetric strain tensor, with a color LUT scale ranging from ±100% for the strain fields and rotations of ±1 rad for the rotation component. These demonstrate negligible strain within the graphene lattice originating from the s-MV defect. Figure 3i−l similarly shows the GPA-calculated strain components for the r-MV shown in Figure 3g. For this defect configuration, the area immediately surrounding the defect exhibits a pronounced strain, notably different from the s-MV case. This result is supported by the results from *ab initio* calculations, where the necessary bond reconstruction is known to create a strain in the surrounding graphene lattice.[39] The two MV configurations can also be compared directly by considering the relative atomic displacement between the pristine and defective graphene lattices, as shown in Figure S2. In this analysis, the r-MV defect exhibits a stronger displacement field than the s-MV, supporting the GPA results.

Figure 4a shows a smoothed AC-TEM image of an r-MV, with the inset showing a magnified view. The improved resolution in this image compared to the other AC-TEM images shown here, which enables the visualization of individual carbon atoms, is due to the use of a monochromated electron beam. In Figure 4b, gray scale intensity profiles are shown, labeled (i−iii), taken between the three edge atoms of the MV, with (i) corresponding to the reconstructed bond. These show that the reconstructed bond length is 1.9 Å, in good agreement with our calculations which yield 1.90 Å. The distances between the edge atoms that are not bonded were measured to be 2.8 ± 0.1 Å. In Figure 4c, a smoothed, non-monochromated AC-TEM image of a s-MV is shown, accompanied by a magnified view inset. Intensity line profiles between the edge C atoms are shown in Figure 4d, with measured distances between 2.3 and 2.6 Å, compared to theoretical predictions of 2.44 Å, which is a minor deviation from the pristine lattice case of 2.46 Å.

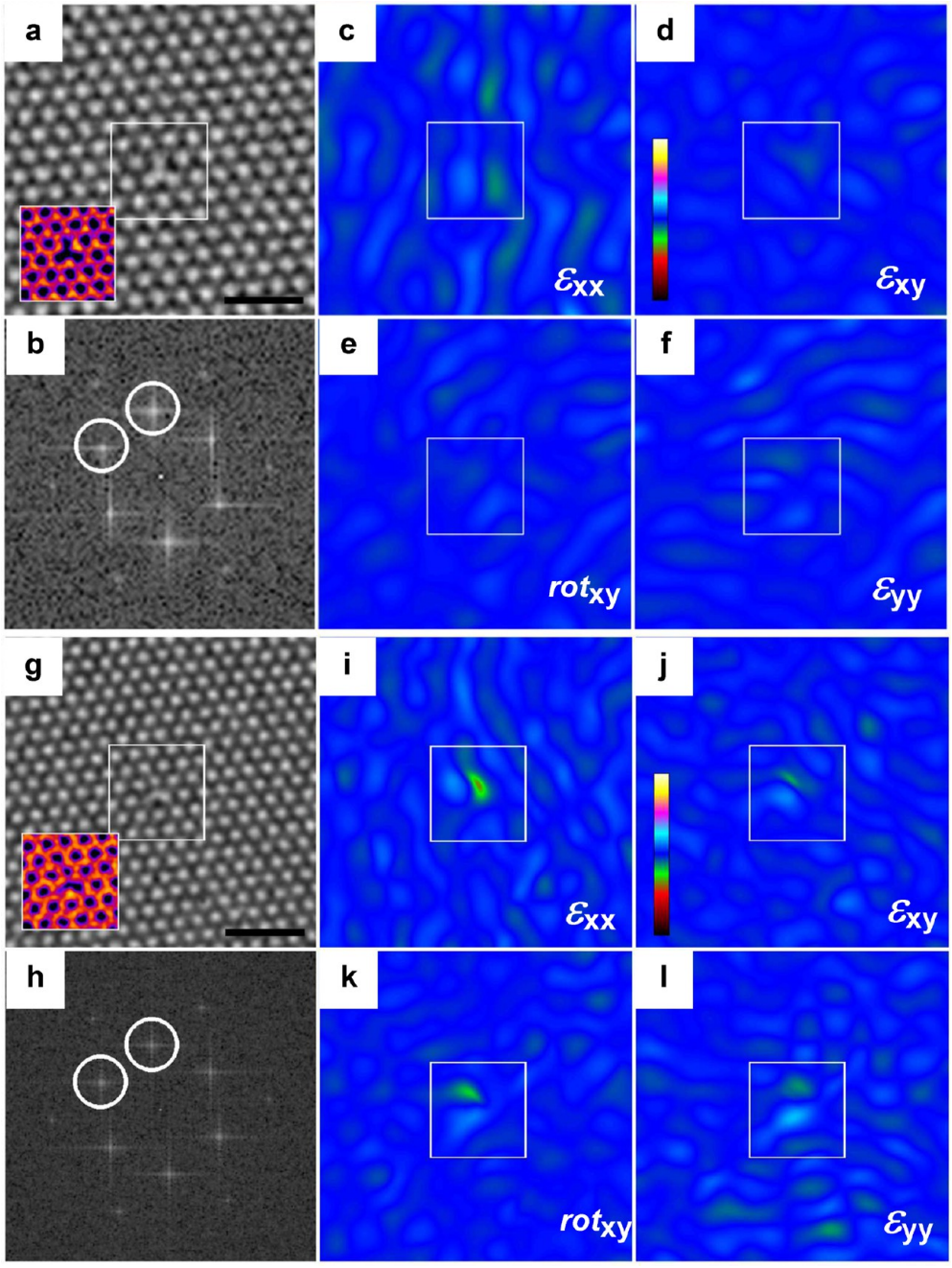

Figure 3. Geometric phase analysis (GPA) for the two monovacancy bonding configurations. (a) Smoothed AC-TEM image of the s-MV used for calculating the GPA maps, with the inset showing a smoothed color LUT image of the vacancy region. (b) FT of (a), with the two {100} reflections used to calculate the phase maps circled. (c−f) Calculated fields of the symmetric strain matrix around the s-MV, with the elements (ε_{xx}, ε_{xy}, rot_{xy}, and ε_{yy}) labeled. (g) Smoothed AC-TEM image of the r-MV used for calculating the GPA maps, with the inset showing a smoothed color LUT image of the vacancy region. (h) FT of (g), with the two {100} reflections used to calculate the phase maps circled. (i−l) Calculated strain matrix elements around the s-MV. In all cases, scale bars denote 1 nm. The CLUT palette used covers the range of ±100% for the strain fields and ±1 radians for the rotations, with blue corresponding to zero.

In Figure 4e, an average of three consecutive AC-TEM images of a r-MV is shown, which was executed to improve atomic contrast and was possible due to minimal variation in the beam astigmatism between exposures. This image shows the three atoms opposite the bond reconstruction, which includes the under-coordinated carbon, with sufficient clarity to use intensity line profiles to extract the bond lengths of the carbon radical. These line profiles, taken across the appropriate armchair axes to include both the under-coordinated C bond and C−C bonds from the bulk lattice, are shown in Figure 4f. From these, we find a bond compression to 1.37 and 1.21 Å for the bonds lying along armchair axes labeled (i) and (ii), respectively. These deviate from the bulk C−C bond lengths, found from the same plots, of 1.52 ± 0.02 and 1.58 ± 0.02 Å,

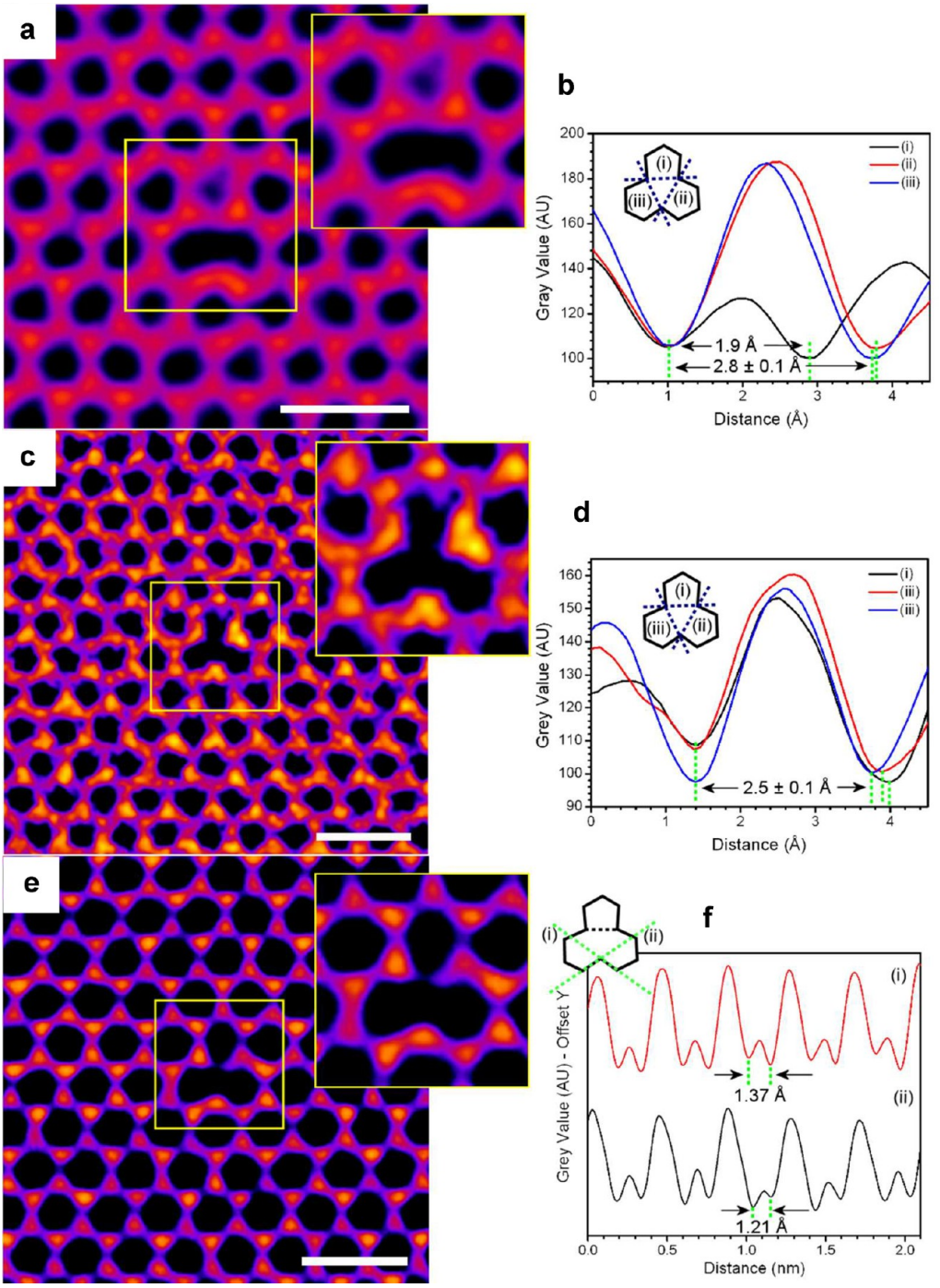

Figure 4. (a) Smoothed AC-TEM image of a r-MV, with the highlighted region around the defect magnified in the inset. (b) Intensity line profiles (i−iii) measured between edge atoms of the MV along three axes, as illustrated in the inset. (c) Smoothed AC-TEM image of a s-MV, and a magnified view of the defect inset. (d) Intensity line profiles (i−iii) measured for the interatomic distances between the three edge atoms along the three axes as illustrated in the inset. (e) Average of three consecutive r-MV AC-TEM images, and a magnified view of the r-MV inset. (f) Line profiles taken along two of the armchair axes, (i) and (ii), as shown in the inset schematic. These axes each cross one of the compressed C−C bonds with the under-coordinated C atom of the r-MV. Scale bars denote 0.5 nm.

yielding a respective bond compression of 77 and 90% for the two cases. However, it is important to note that the nature of AC-TEM imaging physically precludes the measurement of any bond length contribution in the *z*-axis; thus any out-of-plane displacement of the under-coordinated C would lead to an illusory bond compression in the TEM image, due to it corresponding to the projection of the bond into the 2D *x*−*y* plane.

From theoretical studies, the migration of monovacancies in graphitic materials is thought to occur by a switching mechanism.[15,16,21] In this mechanism, one of the vacancy edge atoms switches to the opposite side

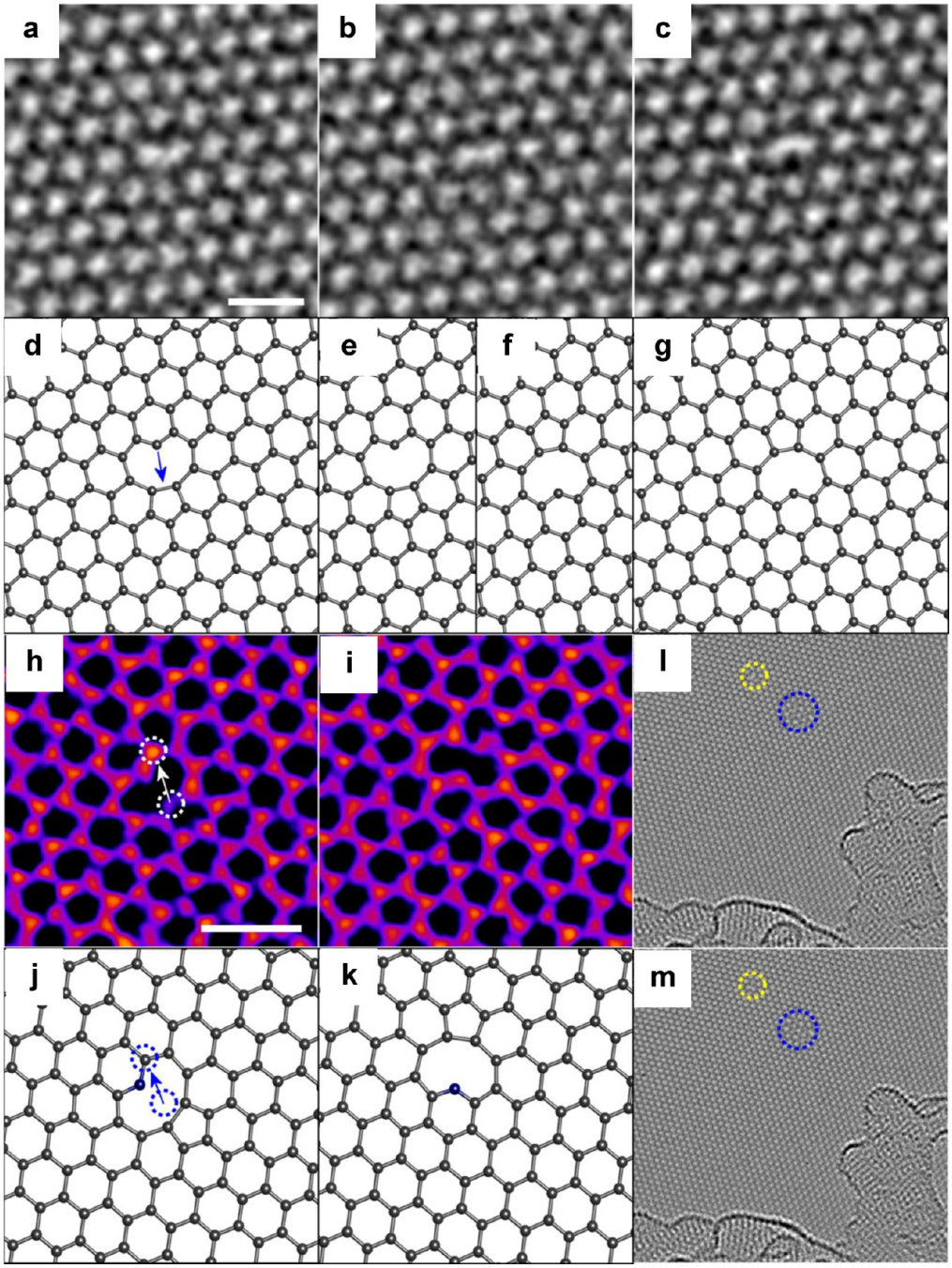

Figure 5. (a) Smoothed AC-TEM image of a r-MV, which switches lattice positions *via* an intermediate position, shown in (b), resulting in a new translated r-MV (c). (d−g) Atomistic models corresponding to the images shown in (a−c), respectively, with (e) and (f) showing models illustrating the superposition proposed for the image in (b). (h,i) Color LUT of smoothed AC-TEM images of a r-MV undergoing a lattice shift. The dashed white circles show the migration of the vacancy. (j,k) Atomistic models corresponding to the AC-TEM images shown in (h,i), respectively. The dark blue highlighted atom is fixed during the transition, and the dashed blue circles indicate the migration of the vacancy. (l,m) Wide field AC-TEM images, from which (h,i) were extracted, with the r-MV defect highlighted by the yellow circle. The blue circle highlights a more complex defect used as an alignment marker to compensate for drift between the two images. Scale bars in all cases are 0.5 nm.

of the vacancy, thus shifting the vacancy to an adjacent lattice position. This has been observed in our experimental images (Figure 5a−c). Figure 5a shows a smoothed AC-TEM image of a r-MV, with an accompanying atomistic model in Figure 5d. The blue arrow in the schematic illustrates the motion of the unsaturated C atom, which breaks the reconstructed bond on the opposite side of the MV, leading to the configuration observed in Figure 5c and modeled in Figure 5g. In between these two frames, an intermediate frame was captured (Figure 5b). We hypothesize that this image is a superposition of the configurations shown in Figure 5e,f. It was found that for two of the three observed occurrences of this migration there was an

intermediate superposition frame, with a straight switch for the third. In addition to this expected migration, we have also observed vacancy migration by one zigzag lattice plane. Figure 5h,i shows smoothed AC-TEM images, captured with a monochromated beam, of a r-MV undergoing this lattice transition. The dashed white circles and arrow indicate the migration path of the vacancy, with equivalent dashed blue annotations shown on the atomistic model in Figure 5j. The atom highlighted in dark blue in the atomistic models of Figure 5j,k appears to remain fixed, while the vacancy structure rotates about it. However, in order to be certain that the vacancy has actually shifted lattice positions, rather than the bond reconstruction merely re-forming between one of the two remaining pairs of under-coordinated C radicals in the same vacancy and the shift appearing due to sample drift, it was crucial to align the two images with respect to other common features. In Figure 5l,m, a wide field view around the defects is shown, with Figure 5l,m corresponding to blown-up views of Figure 5h,i, respectively. The r-MV is highlighted by the yellow dashed circle, and the images were aligned with reference to the larger defect cluster, highlighted by the blue dashed circle and to the amorphous carbon residue along the lower part of the image. Using these features to align the images, in order to compensate for sample drift, it is clear that the transition observed corresponds to a lattice transition, rather than just a rotation of the reconstruction about the vacancy. This migration type was observed to occur 13 times in our data set, significantly more frequently than for the simple switching mechanism in Figure 5a–c. All of these lattice shifts were imaged to occur immediately in the subsequent exposure, with no intermediate superposition state recorded.

Our failure to observe the r-MV swapping the reconstructed bond around the vacancy site, as proposed to explain the observation of s-MV in STM images by ref 20, and discussed earlier, is somewhat surprising, as the same reference also suggests a low energy barrier for the bond alternation of 0.13 eV. For such an energy barrier, one would expect bonding switches to occur readily under the electron beam. It is possible that the lack of observed reconstruction swapping is due to the under-coordinated C atom (highlighted in dark blue in Figure 5j,k) being functionalized by a low mass contaminant, such as hydrogen, precluding the formation of a third sp^2 bond and preventing any oscillation of the reconstruction. In this model, the under-coordinated C atom in the r-MV is effectively saturated, offering an explanation as to why the reconstructed bond is not observed to alternate between the three edge C atoms of the MV. This hypothesis can be extended by including the results shown in Figure 2, which demonstrated that it was not possible to differentiate by AC-TEM between an oscillating r-MV and a s-MV: It is therefore possible that the imaged s-MVs are oscillating r-MVs, and the r-MVs we image have been stabilized from oscillation by the functionalization of the under-coordinated C radical. If this is indeed the case, it may be possible to observe a deviation in the length of the nearby C–C bonds, which presents a promising avenue for further research; however, the AC-TEM here cannot be used to categorically confirm bond compression due to the imaging of the projection of an out-of-plane displacement onto a 2D plane leading to a perspective induced shortening. Evidence to support the functionalization hypothesis may be obtained in the future by employing techniques such as atomic resolution electron energy loss spectroscopy (EELS).

CONCLUSION

We have characterized monovacancy structures in graphene using AC-TEM imaging and have observed two configurations for the monovacancy; the symmetric (s-MV) and the reconstructed monovacancy (r-MV). Geometric phase analysis and bond length measurements have demonstrated that these are observations of two distinct defect types, with the reconstruction giving rise to pronounced strain and displacement in the surrounding lattice. We have also explored mechanisms by which the observed s-MV could be a superposition of an oscillating r-MV, and find that it is not possible to distinguish between them. However, the observation of stable r-MV over extended exposures either suggests the stable existence of two defect types, the s-MV and the r-MV, or that functionalization of an under-coordinated C radical may act to lock the oscillating r-MV into a stable configuration that can be subsequently imaged. These studies shed light on our understanding of defect structures and their behavior in the graphene lattice, which is fundamental to the development of doping and nanoengineering techniques.

METHODS

Graphene was synthesized according to the liquid copper catalyst chemical vapor deposition method outlined in ref 30. Copper foil was placed on top of a molybdenum surface, inserted into a furnace, and subjected to a 30–60 min anneal at 1090 °C under Ar (200 sccm) and H_2/Ar mix (25% H_2 at 100 sccm) gas flow, melting the copper. H_2/Ar mix flow was reduced to 80 sccm, and CH_4/Ar mix (1% CH_4) was set at 10 sccm flow for 90 min. The sample was removed and rapidly cooled at ambient temperature under a H_2 and Ar atmosphere. Transfer was accomplished by using a PMMA scaffold applied to the graphene/Cu/Mo stack before floating on $FeCl_3$ etchant to remove the PMMA/graphene from the metal, followed by HCl and DI water rinse stages. The PMMA/graphene film was then

transferred to a holey silicon nitride TEM grid. The PMMA was subsequently removed by baking in ambient atmosphere at 350 °C overnight. Prior to TEM imaging, the sample was heated under vacuum at ~150 °C using a filament heater to remove residual surface contamination.

Conflict of Interest: The authors declare no competing financial interest.

Acknowledgment. A.W.R. was funded by an EPSRC studentship. C.S.A. acknowledges funding from EPSRC Grant EP/H001972/1. J.H.W. thanks the support from the Royal Society and Balliol College.

Supporting Information Available: Supplementary figures showing displacement maps of s-MV and r-MV and AC-TEM image series of a r-MV. This material is available free of charge *via* the Internet at http://pubs.acs.org.

REFERENCES AND NOTES

1. Novoselov, K. S.; Fal'ko, V. I.; Colombo, L.; Gellert, P. R.; Schwab, M. G.; Kim, K. A Roadmap for Graphene. *Nature* **2012**, *490*, 192–200.
2. Schwierz, F. Graphene Transistors. *Nat. Nanotechnol.* **2010**, *5*, 487–496.
3. Britnell, L.; Gorbachev, R. V.; Jalil, R.; Belle, B. D.; Schedin, F.; Mishchenko, A.; Georgiou, T.; Katsnelson, M. I.; Eaves, L.; Morozov, S. V.; *et al.* Field-Effect Tunneling Transistor Based on Vertical Graphene Heterostructures. *Science* **2012**, *335*, 947–950.
4. Fahey, P. M.; Griffin, P. B.; Plummer, J. D. Point Defects and Dopant Diffusion in Silicon. *Rev. Mod. Phys.* **1989**, *61*, 289–384.
5. Tang, M.; Colombo, L.; Zhu, J.; Diaz de la Rubia, T. Intrinsic Point Defects in Crystalline Silicon: Tight-Binding Molecular Dynamics Studies of Self-Diffusion, Interstitial-Vacancy Recombination, and Formation Volumes. *Phys. Rev. B* **1997**, *55*, 14279–14289.
6. Hahn, J.; Kang, H.; Song, S.; Jeon, I. Observation of Charge Enhancement Induced by Graphite Atomic Vacancy: A Comparative STM and AFM Study. *Phys. Rev. B* **1996**, *53*, R1725–R1728.
7. Hahn, J.; Kang, H. Vacancy and Interstitial Defects at Graphite Surfaces: Scanning Tunneling Microscopic Study of the Structure, Electronic Property, and Yield for Ion-Induced Defect Creation. *Phys. Rev. B* **1999**, *60*, 6007–6017.
8. Kelly, K. F.; Sarkar, D.; Hale, G. D.; Oldenburg, S. J.; Halas, N. J. Threefold Electron Scattering on Graphite Observed with C60-Adsorbed STM Tips. *Science* **1996**, *273*, 1371–1373.
9. Banhart, F. Irradiation Effects in Carbon Nanostructures. *Rep. Prog. Phys.* **1999**, *62*, 1181–1221.
10. Krasheninnikov, A.; Nordlund, K.; Sirviö, M.; Salonen, E.; Keinonen, J. Formation of Ion-Irradiation-Induced Atomic-Scale Defects on Walls of Carbon Nanotubes. *Phys. Rev. B* **2001**, *63*, 245405.
11. Ma, Y.; Lehtinen, P. O.; Foster, A. S.; Nieminen, R. M. Magnetic Properties of Vacancies in Graphene and Single-Walled Carbon Nanotubes. *New J. Phys.* **2004**, *6*, 68.
12. Lehtinen, P.; Foster, A.; Ma, Y.; Krasheninnikov, A.; Nieminen, R. Irradiation-Induced Magnetism in Graphite: A Density Functional Study. *Phys. Rev. Lett.* **2004**, *93*, 187202.
13. Pereira, V.; Guinea, F.; Lopes dos Santos, J.; Peres, N.; Castro Neto, A. Disorder Induced Localized States in Graphene. *Phys. Rev. Lett.* **2006**, *96*, 036801.
14. Yazyev, O.; Helm, L. Defect-Induced Magnetism in Graphene. *Phys. Rev. B* **2007**, *75*, 125408.
15. Lee, G.-D.; Wang, C.; Yoon, E.; Hwang, N.-M.; Kim, D.-Y.; Ho, K. Diffusion, Coalescence, and Reconstruction of Vacancy Defects in Graphene Layers. *Phys. Rev. Lett.* **2005**, *95*, 205501.
16. Thrower, P. A.; Mayer, R. M. Point Defects and Self-Diffusion in Graphite. *Phys. Status Solidi A* **1978**, *47*, 11–37.
17. Hjort, M.; Stafström, S. Modeling Vacancies in Graphite *via* the Hückel Method. *Phys. Rev. B* **2000**, *61*, 14089–14094.
18. Lim, D.-H.; Negreira, A. S.; Wilcox, J. DFT Studies on the Interaction of Defective Graphene-Supported Fe and Al Nanoparticles. *J. Phys. Chem. C* **2011**, *115*, 8961–8970.
19. El-Barbary, A. First Principles Characterisation of Defects in Irradiated Graphitic Materials. Ph.D. Thesis, University of Sussex, 2005.
20. El-Barbary, A.; Telling, R.; Ewels, C.; Heggie, M.; Briddon, P. Structure and Energetics of the Vacancy in Graphite. *Phys. Rev. B* **2003**, *68*, 144107.
21. Kaxiras, E.; Pandey, K. Energetics of Defects and Diffusion Mechanisms in Graphite. *Phys. Rev. Lett.* **1988**, *61*, 2693–2696.
22. Sammalkorpi, M.; Krasheninnikov, A.; Kuronen, A.; Nordlund, K.; Kaski, K. Mechanical Properties of Carbon Nanotubes with Vacancies and Related Defects. *Phys. Rev. B* **2004**, *70*, 245416.
23. Hashimoto, A.; Suenaga, K.; Gloter, A.; Urita, K.; Iijima, S. Direct Evidence for Atomic Defects in Graphene Layers. *Nature* **2004**, *430*, 870–873.
24. Meyer, J. C.; Kisielowski, C.; Erni, R.; Rossell, M. D.; Crommie, M. F.; Zettl, A. Direct Imaging of Lattice Atoms and Topological Defects in Graphene Membranes. *Nano Lett.* **2008**, *8*, 3582–3586.
25. Gass, M. H.; Bangert, U.; Bleloch, A. L.; Wang, P.; Nair, R. R.; Geim, A. K. Free-Standing Graphene at Atomic Resolution. *Nat. Nanotechnol.* **2008**, *3*, 676–681.
26. Robertson, A. W.; Allen, C. S.; Wu, Y. A.; He, K.; Olivier, J.; Neethling, J.; Kirkland, A. I.; Warner, J. H. Spatial Control of Defect Creation in Graphene at the Nanoscale. *Nat. Commun.* **2012**, *3*, 1144.
27. Huang, P. Y.; Ruiz-Vargas, C. S.; van der Zande, A. M.; Whitney, W. S.; Levendorf, M. P.; Kevek, J. W.; Garg, S.; Alden, J. S.; Hustedt, C. J.; Zhu, Y.; *et al.* Grains and Grain Boundaries in Single-Layer Graphene Atomic Patchwork Quilts. *Nature* **2011**, *469*, 389–392.
28. Chen, J.-H.; Li, L.; Cullen, W. G.; Williams, E. D.; Fuhrer, M. S. Tunable Kondo Effect in Graphene with Defects. *Nat. Phys.* **2011**, *7*, 535–538.
29. Warner, J. H.; Margine, E. R.; Mukai, M.; Robertson, A. W.; Giustino, F.; Kirkland, A. I. Dislocation-Driven Deformations in Graphene. *Science* **2012**, *337*, 209–212.
30. Wu, Y. A.; Fan, Y.; Speller, S.; Creeth, G. L.; Sadowski, J. T.; He, K.; Robertson, A. W.; Allen, C. S.; Warner, J. H. Large Single Crystals of Graphene on Melted Copper Using Chemical Vapor Deposition. *ACS Nano* **2012**, *6*, 5010–5017.
31. Cowley, J. M.; Moodie, A. F. The Scattering of Electrons by Atoms and Crystals. I. A New Theoretical Approach. *Acta Crystallogr.* **1957**, *10*, 609–619.
32. Perdew, J. P.; Burke, K.; Ernzerhof, M. Generalized Gradient Approximation Made Simple. *Phys. Rev. Lett.* **1996**, *77*, 3865–3868.
33. Dovesi, R.; Saunders, V. R.; Roetti, C.; Orlando, C.; Zicovich-Wilson, C. M.; Pascale, F.; Civalleri, B.; Doll, K.; Harrison, N. M.; Bush, I. J.; *et al. CRYSTAL09 User's Manual*; University of Torino: Torino, Italy, 2009.
34. Dovesi, R.; Orlando, R.; Civalleri, B.; Roetti, C.; Saunders, V. R.; Zicovich-Wilson, C. M. CRYSTAL: A Computational Tool for the *Ab Initio* Study of the Electronic Properties of Crystals. *Z. Kristallogr.* **2005**, *220*, 571–573.
35. Pisani, L.; Montanari, B.; Harrison, N. Stability of the Ferromagnetic State in a Mixed sp^2-sp^3 Carbon System. *Phys. Rev. B* **2009**, *80*, 104415.
36. Liu, Z.; Suenaga, K.; Harris, P.; Iijima, S. Open and Closed Edges of Graphene Layers. *Phys. Rev. Lett.* **2009**, *102*, 015501.
37. Hytch, M. J.; Snoeck, E.; Kilaas, R. Quantitative Measurement of Displacement and Strain Fields from HREM Micrographs. *Ultramicroscopy* **1998**, *74*, 131–146.
38. Hytch, M. J.; Putaux, J.-L.; Pénisson, J.-M. Measurement of the Displacement Field of Dislocations to 0.03 A by Electron Microscopy. *Nature* **2003**, *423*, 270–273.
39. Hunt, M.; Clark, S. Extraordinarily Long-Ranged Structural Relaxation in Defective Achiral Carbon Nanotubes. *Phys. Rev. Lett.* **2012**, *109*, 265502.